Sensors and Materials, Vol. 36, No. 1 (2024) 235–249
MYU Tokyo

S & M 3514

Micro X-ray Computed Tomography and Machine Learning Assessment of Impregnation Efficacy of Die-Casting Defects in Metal Alloys

Ajith Bandara,[1*] Koichi Kan,[1] Katanaga Yusuke,[1,2] Natsuto Soga,[1,2]
Takagi Katsuyuki,[3,4] Akifumi Koike,[3] and Toru Aoki[2,4]

[1]Hamamatsu TSC, Chuo Hatsumei Institute, 322 Iida-cho, Minami-ku, Hamamatsu 435-0028, Japan
[2]Graduate School of Medical Photonics, Shizuoka University,
Johoku 3-5-1, Hamamatsu, Shizuoka 432-8561, Japan
[3]ANSeeN Inc., Johoku 3-5-1, Hamamatsu, Shizuoka 432-8561, Japan
[4]Research Institute of Electronics, Shizuoka University, Johoku 3-5-1, Hamamatsu, Shizuoka 432-8561, Japan

(Received September 30, 2023; accepted November 22, 2023)

Keywords: micro X-ray computed tomography, direct conversion X-ray sensors, machine learning image segmentation, Al-alloy die-casting, vacuum pressure impregnation, dual-energy X-ray CT

Die-cast light metal alloys in various industrial applications require precise airtightness, and vacuum pressure impregnation (VPI) is typically used to seal casting defects to ensure product reliability. Evaluating the efficacy of VPI in sealing alloy defects is crucial. In this study, laboratory-based micro X-ray computed tomography (micro-XCT) was effectively employed in conjunction with advanced direct conversion CdTe semiconductor sensors to nondestructively evaluate the efficacy of standard VPI in sealing die-casting defects of industrial Al alloys. The internal casting defects and the low-atomic-number impregnation sealant distribution were visualized by adjusting the scalar opacity mapping in 3D CT. In 2D CT, it is challenging to identify the sealant resin in the narrow leakage paths of the alloy sample due to its low grey contrast, and a machine learning approach with the Trainable Weka Segmentation (TWS) plug-in was applied to segment the CT images more precisely than by the traditional intensity-based image processing technique. TWS efficiently segmented the Al alloy, air pores, and diffused sealant resin in the samples, providing an in-depth analysis of the impregnation efficacy. Dual-energy XCT (DXCT) with photon-counting sensors was utilized as a quantitative method based on the effective atomic number to identify the impregnation material in the alloys as the commercially used Super Sealant P601 polymer resin.

1. Introduction

X-ray computed tomography (XCT) has become a broad and effective nondestructive imaging technique used in the medical and industrial sectors since the first commercial CT scanner was built for medical imaging by Nobel Prize winner Godfrey Hounsfield in 1969.[1,2]

*Corresponding author: e-mail: chuhatsu.gkc1@gmail.com
https://doi.org/10.18494/SAM4675

ISSN 0914-4935
https://myukk.org/

With the rapid development of CT technology, computer performance, and software, XCT in the industrial field has become well known for its faster and more cost-effective investigation than traditional evaluation methods.[3] As a robust nondestructive testing (NDT) method, XCT is increasingly widely used in various industrial sectors, particularly the automotive, aerospace, and material industries.[4,5]

In XCT, X-ray radiation attenuates owing to physical mechanisms such as the photoelectric effect and elastic or inelastic scattering, leading to a reduction in intensity as it penetrates the sample of interest.[6-8] After penetration, multiple 2D projection images on an image sensor are captured from various angles while the sample is rotated to record the X-ray intensity distribution.[9] A model of the object is then reconstructed using dedicated image processing software, enabling a comprehensive qualitative and quantitative analysis of the object's external and internal structures.

CT is now used for material analysis, internal flaw detection, dimensional metrology, assembly analysis, and reverse engineering applications.[10,11] Furthermore, its capacity to capture numerous complete tomograms per second enables the real-time examination of sample transformations resulting from reactions or applied processing operations.[12]

We have been investigating the efficacy of the impregnation technique in sealing die-casting defects of light metal alloys. Such die-cast alloys are widely used for intricate industrial parts, especially in automotive, owing to advantages including reduced weight, enhanced fuel efficiency, corrosion resistance, high strength-to-weight ratio, thermal conductivity, and recyclability, thus contributing to sustainability and reducing environmental impact.[13-18] However, the use of high-pressure die-casting (HPDC) in producing automotive light-alloy castings generates scraps due to defects such as gas pores and shrinkage cracks.[19,20] Interconnected pores and leakage paths in light alloys often result in the leakage of gases, liquids, and oil. These defects can adversely affect casting products and ultimately lead to reduced performance and reliability.[21] Despite several advances in die-casting technology, completely eliminating defects remains a significant challenge. Hence, impregnation treatments are applied as a cost-effective means of sealing pores and eliminating leakage paths to ensure the quality of cast components.[22-25] Nevertheless, the current standard dipping water leak test is inadequate to ensure impregnation efficacy , and a reliable, nondestructive imaging technique is required.

In this study, we investigate the efficacy of vacuum pressure impregnation (VPI) in sealing Al alloy die-casting (ADC12) defects using a laboratory-based semi-automated micro-XCT, effectively using high-performance flat panel detectors (FPDs) based on a cadmium telluride (CdTe) compound semiconductor crystal as the sensor material for qualitative and quantitative analyses. These sensors operate through direct conversion, enabling robust detection. Whereas micro-XCT has been extensively applied as an NDT method for analyzing the structure and imperfections of metal alloys,[26-30] its potential for visualizing and characterizing impregnation resin within sealed casting defects remains largely unexplored. This is due to the resin's low atomic number and mass density, resulting in reduced X-ray attenuation.[31] Consequently, its detection in CT images is challenging owing to increased X-ray beam hardening and decreased attenuation caused by higher-energy X-ray photons. The impregnation resin primarily remains

within a confined region of the casting defect, further complicating the acquisition of CT images with adequate contrast and spatial resolution.

XCT analysis with advanced pixeled Pt/CdTe/In sensors is suitable for creating high-resolution 2D and 3D CT images. This technique facilitates the precise characterization and evaluation of internal defects, including the nondestructive assessment of the impregnation efficacy of Al alloy die-casting. The portable FPDs present several distinct advantages, such as higher X-ray conversion efficiency over scintillating materials, energy differentiation via photon counting, diffusion-free imaging, fast processing with LSI, and gapless tiling.

In the micro-XCT study, we used three distinct ADC12 samples, each possessing nearly identical dimensions. Three-dimensional CT imaging effectively facilitated the visualization of internal casting defects such as gas pores and gas-filled cracks within the ADC samples. By adjusting the scalar opacity mapping, we successfully depicted the distribution of the low-atomic-number and low-density impregnation resin in the ADC samples. The qualitative identification of sealant resin within die-casting defects was achieved by analyzing the grey contrast variation in 2D CT slice images. Given the limitations of conventional intensity-based segmentation in accurately detecting impregnation resin, we employed a machine learning (ML) approach using the Trainable Weka Segmentation (TWS) tool. TWS is a plug-in of the Fiji image analysis software and has proven to be functional and accurate for performing segmentation in various imaging pipelines and across many image modalities. Notably, it has been employed successfully in applications such as visualizing myocardial blood flow,[32] micro- and computerized tomography,[33-35] and, most recently, in the analysis of micro X-ray CT images of Al alloys conducted by our research group.[25] By training the known datasets, this approach precisely segmented the Al alloy, air pores, and resin materials within the casting defects of the samples.

The 2D CT analysis effectively detected the successfully sealed narrow leakage pathways. However, upon the examination of cross-sectional CT images, we noticed that the leakage pathway of Al alloy sample 3 had not been fully sealed during the VPI process. The sealant resin was found only within a confined region of the leakage path. Furthermore, we used a quantitative method employing a photon-counting CdTe sensor to identify the impregnation resin material in casting defects and Al alloys. The calculated effective atomic number (EAN) based on the linear attenuation coefficients was used to identify the impregnation sealant as the industrially utilized Super Sealant P601.

Because of the fast data processing and straightforward sample preparation and handling, laboratory-based micro-XCT with advanced CdTe sensors enables the comprehensive and nondestructive assessment of the casting defects and impregnation treatment of metal alloys. Thus, our findings provide valuable insights for enhancing both the VPI technique parameters and the properties of the sealant resin to improve quality assurance for impregnation.

2. Experiments

2.1 Samples and impregnation

Our micro-XCT investigation was conducted using lightweight industrial Al alloy samples. We prepared three cuboidal samples and focused on specific regions of interest (ROIs) within the standard Al alloy test pieces, as illustrated in Fig. 1. These samples, composed of ADC12 alloy with a density of 2.74 g/cm³, were manufactured via HPDC and were provided for examination by Mikawa Koki Fukuroi Manufacturing Co., Ltd., Japan. All samples had the same dimensions (10 × 10 × 5 mm^3) and were impregnated by a standard VPI technique before the XCT investigation. In addition to the inherent casting defects, sample 1 featured an artificial hole of approximately 0.6 mm diameter at its center.

The standard VPI technique (MIL-STD-276A Method B) was performed using a highly efficient thermosetting polymer solution, commercially known as Super Seal P601 (Chuo Hatsumei Institute Co., Ltd., Japan), for impregnation. The primary composition of this colorless transparent sealing mixture includes the 2-hydroxyethyl methacrylate bifunctional monomer (2-HEMA), which has a viscosity of 6 mPa.s and a density of 1.06 g/cm^3 at 25 °C. Aluminum alloy samples were placed in a vacuum vessel that was evacuated to 65 Pa for 5 min, eliminating air and moisture. Impregnating resin was introduced while maintaining a vacuum for 15 min to fill gaps and pores. Then, the vessel pressure was increased to 0.4 MPa using dry air, enhancing resin penetration. The excess resin was drained after pressure release. Next, the samples were washed lightly by dipping them in water and then precured in hot water. Finally, the alloy samples were heated to 95 ºC for 1 h in an oven to harden the resin through cross-linked polymerization. Similarly, the center hole of sample 1 was impregnated manually using P601 Super Seal resin; then, the sample was kept at 95 °C for 1 h to induce polymerization. The prepared samples were used for XCT measurements.

2.2 Analytical methods

Two different XCT methods were employed to assess the die-casting defects and the effectiveness of impregnation. A qualitative analysis was initially conducted using a cutting-edge charge-integration-type pixeled CdTe X-ray sensor (ANSeeN Inc., Hamamatsu). Then, a dual-energy XCT (DXCT) quantitative analysis using a CdTe-based photon-counting XCounter

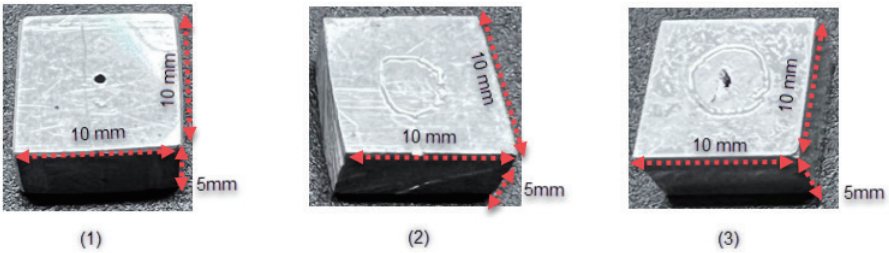

Fig. 1. (Color online) Images of die-cast Al alloy test samples.

sensor (XC-Hydra-FX20, Direct Conversion AB, Sweden) was executed to identify the impregnation material in the Al-casting defects as Super Seal P601. A laboratory-based semi-automated XCT system with a microfocus X-ray source (L12161-07, Hamamatsu) was used for X-ray generation.

2.2.1 Qualitative analysis

Projection images of the impregnated ADC12 samples were recorded on a charge-integration-type CdTe sensor-based FPD in the form of a 14-bit greyscale by rotating the sample stage by 360° in 4°/s steps. We used a Schottky diode-type FPD with a pixel pitch of 100 μm that contained a pixel array of 252 rows and 1024 columns. We calibrated the FPD for five different X-ray tube currents before acquiring the projection data of the alloy samples, and we recorded 2700 projection images of each sample at 30 frames per second. The X-ray source-to-sensor distance was set to 550 mm, and a source-to-sample distance of 265 mm was found to achieve an appropriate field of view (FOV) for the Al alloy samples. All projection images were captured using an X-ray tube set at 140 kV and 250 μA, with a focal spot size of 50 μm. A 0.2-mm-thick Cu filter was also employed to mitigate beam-hardening artifacts. A cone-beam CT geometry (CBCT) was employed in the experiment, as depicted in Fig. 2. CT cross-sectional slice images for each sample were reconstructed from their projection images using custom-developed CBCT software employing the filtered back projection algorithm (FBP).[36,37]

The 2D and 3D CT images of ADC12 samples were comprehensively analyzed using Fiji and 3D Slicer image processing software.[38,39] The image quality measure (Q) was calculated to assess the degree of separation between ADC12, P601 resin, and air from the grey-value histogram of the XCT image.[40] We also applied the TWS ML-based image segmentation tool, utilizing supervised modes with a Random Forest classifier,[41] for a more precise segmentation of the 2D CT images than for the conventional intensity-thresholding methods. The TWS model with known data points representing the three classes of ADC12, air, and impregnation sealant regions of the CT image of sample 1 was pretrained interactively. The data points of the sealant used for training were explicitly extracted from the center hole, where we used the P601 Super Sealant impregnation resin for sealing. The trained classifier was saved and applied to 2D CT

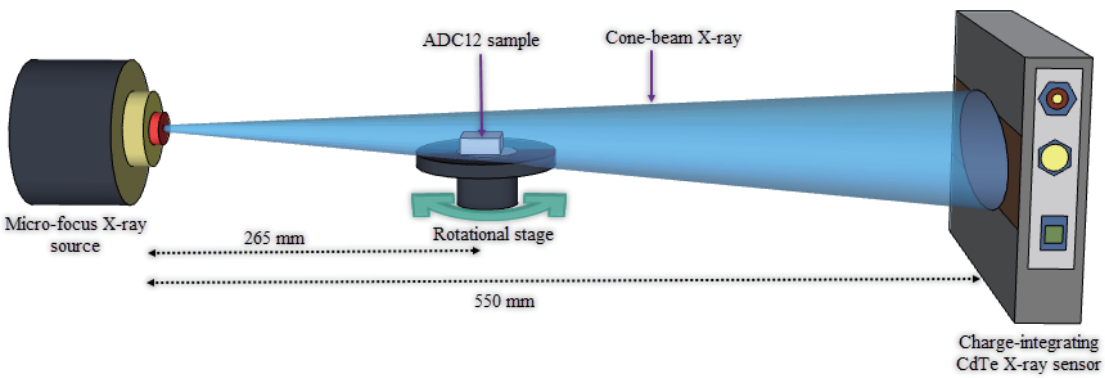

Fig. 2. (Color online) Experimental setup of the charge integration-type CdTe sensor-based FPD.

images of samples 2 and 3. In our study, we could complete the segmentation of the whole image within around 6262 ms, 4451 ms for the finished training, and 1811 ms for classifying whole image data. However, the data processing time will depend on the number of pixels selected for each class, selected training features, and the computer performances. Transparent 3D CT images of the alloy samples were obtained by optimizing the scalar opacity mapping; in a 3D CT volumetric image, the opacity of each voxel intensity can be adjusted by modifying the scalar opacity transfer function in the volume-rendering module. For 3D Al alloy images, we manually reduced the intensities of higher-value voxels (representing the Al alloy material) to show the interior of the image, emphasizing the air pores and the low-atomic-number impregnation resin. The voxel values of the resin material were between those of the air and the alloys. Hence, carefully adjusting the intensity values enabled us to visualize the resin distribution within the Al alloy samples. However, since these threshold values were manually optimized, user adjustment was required to obtain the finer details of images.

2.2.2 Quantitative analysis

In the DXCT analysis, a photon-counting XCounter sensor was used to identify the P601 Super Sealant as the impregnation material on the basis of its EAN. In the sensor, 100 μm CdTe pixel arrays are arranged in a matrix of 64 rows and 2048 columns. After calibration of the XCounter for the background data using its built-in function, projection images of an ROI in sample 1 were captured with a rotation rate of 4°/s over 360°. Figure 3 illustrates the experimental setup utilizing a CBCT geometry with an X-ray generation set at 140 kV/250 μA.

We acquired 2700 projection images for four distinct X-ray energy thresholds (above 20, 30, 50, and 60 keV), defined using the XCounter's operating software. Then, CT images with low-energy (20–30 keV) and high-energy (50–60 keV) windows were constructed using FBP. The EANs of the Al alloy and the impregnated resin located in the center hole and the surrounding die-casting defects of sample 1 were calculated on the basis of their linear attenuation coefficient for the low- and high-energy windows using Eq. (1).[42,43] These derived EANs ($Z_{eff(exp)}$) were then compared with their theoretical values ($Z_{eff(th)}$) to identify the impregnation material as the Super Sealant P601. The XMuDat method was used to calculate the theoretical EAN of the P601.[44]

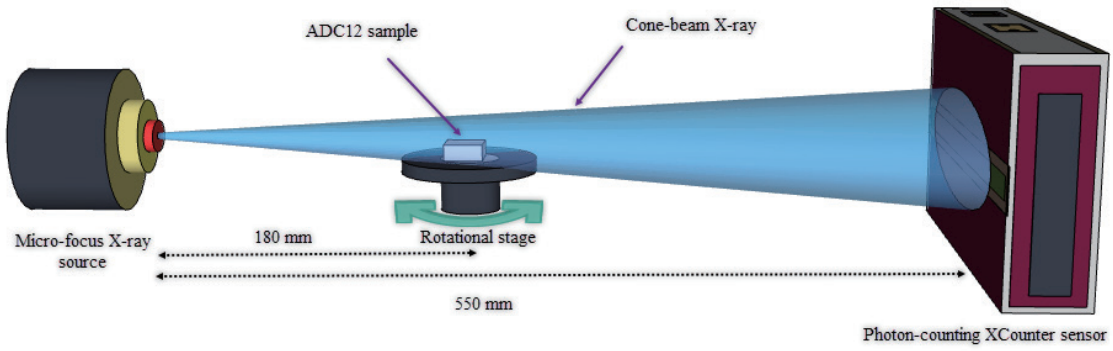

Fig. 3. (Color online) Experimental setup of the photon-counting CdTe sensor-based XCounter FPD.

$$Z^4 = \frac{\mu(E_2)G(E_1, Z) - \mu(E_1)G(E_2, Z)}{\mu(E_1)F(E_2, Z) - \mu(E_2)F(E_1, Z)} \quad (1)$$

Here, $\mu(E_1)$ and $\mu(E_2)$ denote the linear attenuation coefficients associated with low- and high-energy windows, $G(E_1, Z)$ and $G(E_2, Z)$ are the electron cross sections for the scattering term for the two energy windows, and $F(E_1, Z)$ and $F(E_2, Z)$ denote the photoelectric effects within the low- and high-energy windows, respectively.

3. Results and Discussion

3.1 Micro-XCT qualitative analysis

Radiographs of the complete ADC12 sample volume were captured with sufficient magnification, and the 3D CT images were reconstructed to reveal the internal structure and die-casting defects of the alloy samples. The constructed 3D CT images of sample 1 are depicted in Fig. 4.

The greyscale CT image and its scalar opacity mapping image revealed the interior, displaying the center hole and the gas pores formed during casting. The different sizes of the gas pores in the alloy sample can be attributed to various factors during the HPDC process, including the entrapment of hydrogen gas in the molten metal alloy and an excessive amount of lubricant within the die. From the 3D CT scan, only part of the center hole was visible, with the remainder hidden, as highlighted in the side-view 3D image presented in Fig. 4(b). By meticulously fine-tuning the scalar opacity mapping values, we revealed the hidden segment of the center hole and performed a comparative analysis with a cross-sectional 2D CT image, as illustrated in Fig. 5. Figures 5(a) and 5(b) show the hidden part of the center hole in a grey contrast between those of the air pores and Al alloy. In the scalar opacity mapping analysis, we adjusted the Al alloy with a comparatively high density and high atomic number to make it opaque so that the air pores appeared in black and the impregnation resin material with a low density and lower atomic

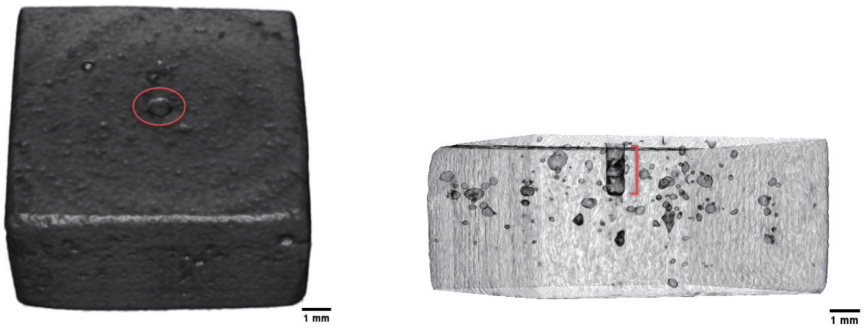

(a) (b)

Fig. 4. (Color online) Three-dimensional CT images of ADC sample 1: (a) greyscale CT image and (b) side-view transparent CT image.

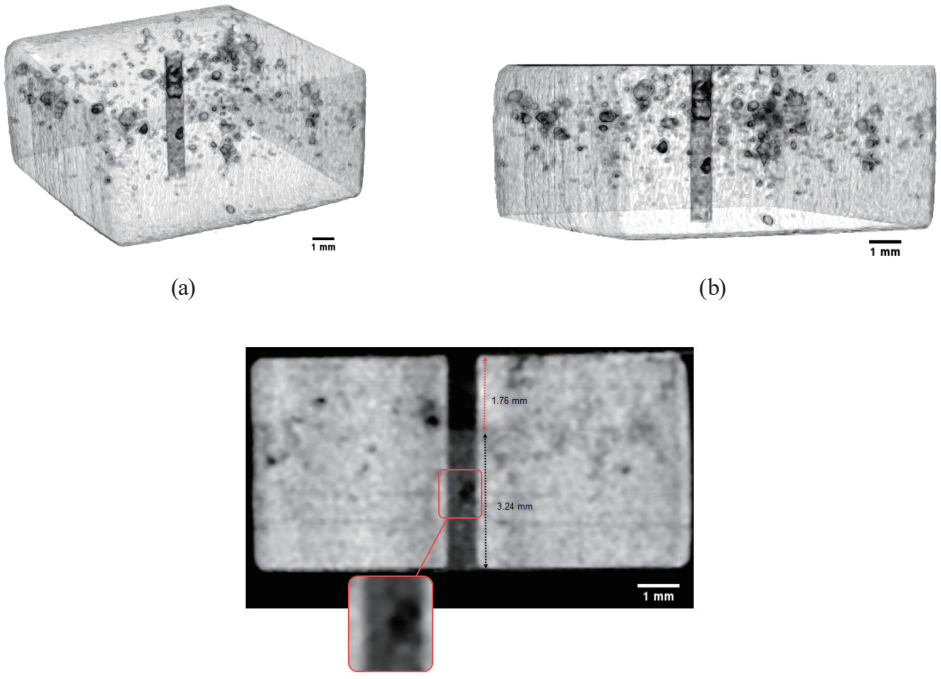

(a) (b)

(c)

Fig. 5. (Color online) XCT images of ADC sample 1: (a) top-view 3D CT image, (b) side-view 3D CT image, and (c) 2D CT image across the center hole.

number appeared in grey contrast. The presence of impregnation resin in the center hole was further indicated by comparing Fig. 5(b) with the cross-sectional 2D CT image in Fig. 5(c). The 2D CT image was well correlated with the 3D image data, revealing the center hole partially sealed with the impregnated resin. There was no resin within 1.76 mm from the top of the hole, and only the bottom 3.24 mm out of the 5.00-mm-deep hole was sealed by the impregnation material.

We also detected a significant air cavity of about 0.110 mm^2 within the impregnated sealant, as depicted in the magnified 2D CT image in Fig. 5(c). Such air cavities reduce the effectiveness of the impregnation. We deviated from the VPI technique by manually injecting the sealant into the center hole of sample 1. Hence, the shrinkage of the sealant during the hardening process and the mixing with the air trapped within the center hole may have impacted the incomplete sealing and air cavity formation within the sealed segment.

Despite our observations of the impregnation material within the relatively large center hole of alloy sample 1 in the CT images, distinguishing sealant in subtle die-casting defects within a sample remains a formidable challenge when using conventional image-thresholding techniques. We calculated the image quality measure (Q) for air–ADC12, ADC12–sealant, and air–sealant using the 2D CT slice image in Fig. 5(c). The impregnation sealant in the center hole was considered in the calculation, and the results are shown in Table 1. The degree of separation between air and the Al alloy ($Q1$) is notably higher than that between the alloy and the impregnation sealant ($Q2$) and between air and the impregnation sealant ($Q3$). Consequently, the

Table 1
Image quality measure for the regions of Al alloy sample 1.

	air–ADC12 ($Q1$)	ADC12–sealant ($Q2$)	air–sealant ($Q3$)
Image quality measure	15.43	8.72	6.26

results suggest that separating the low-density impregnation sealant from the air and the Al alloy is a considerable challenge, particularly when the sealant is within subtle leakage paths. Additionally, the presence of artifacts in the CT image is a further obstacle to resin detection in die-casting defects for ensuring the effectiveness of the VPI in sealing casting defects.

We applied the ML-based image segmentation approach with TWS to the 2D CT image of sample 1, resulting in the segmented CT image shown in Fig. 6. Figure 6(b) presents the segmented image, which clearly visualizes the distribution of the impregnation resin in green within the die-casting defects of Al alloy sample 1. The red color denotes ADC12, whereas the purple color indicates air in the segmented image. As depicted in Fig. 6(a), a subtle, nearly invisible sealed leakage path in the CT image becomes distinctly visible in the ML-based segmented image. However, the complex geometries of leakage paths in die-cast alloys do not consistently follow the same plane, making their complete visualization challenging with cross-sectional 2D CT slices alone.

Analysis of our micro-CT image, as illustrated in Fig. 6(c), effectively revealed the internal microstructure of the Al alloy, indicating its significant advantage as a nondestructive technique. The results confirm the polycrystalline nature of metal alloys, which exhibit a random grain morphology characterized by diverse shapes, sizes, and orientations. The probability map assisted in identifying edges, allowing us to reveal the internal microporosity and cracks in sample 1 more clearly. The previously subtle leakage path is now prominently visible, as highlighted in Fig. 6(c). Additionally, some brighter regions in the probability map image may arise from variation in X-ray linear attenuation due to grain density differences within the alloy sample.

During a leak test, we identified several minor water leakage points on Al alloy sample 2. Remarkably, there was no further leakage after applying the impregnation treatment with the Super Sealant P601. Figure 7 presents a comprehensive visualization of the internal structure indicating the efficacy of the VPI in sealing die-casting defects within the sample. Figure 7(a) illustrates the distribution of micro air pores and the impregnation sealant obtained through scalar opacity mapping in 3D CT, where the highlighted region in the 3D image had more significant leakage.

Figure 7(b) depicts a cross-sectional 2D CT image taken through the highlighted region of the 3D CT, revealing a successfully sealed subtle internal leakage path (20–50 μm) in Al alloy sample 2. The TWS ML-based image segmentation clearly segmented the Al alloy, gas pores, and sealant resin within the sample, as shown in Fig. 7(c). The probability map in Fig. 7(d) provides further details of the geometry of the leakage path and the alloy structure.

Nevertheless, the outcomes of the analysis of casting defects in Al alloy sample 3 emphasized the importance of employing the nondestructive micro-XCT approach to assess impregnation efficacy. Internal gas pores and a significant irregular die-casting crack in alloy sample 3 are

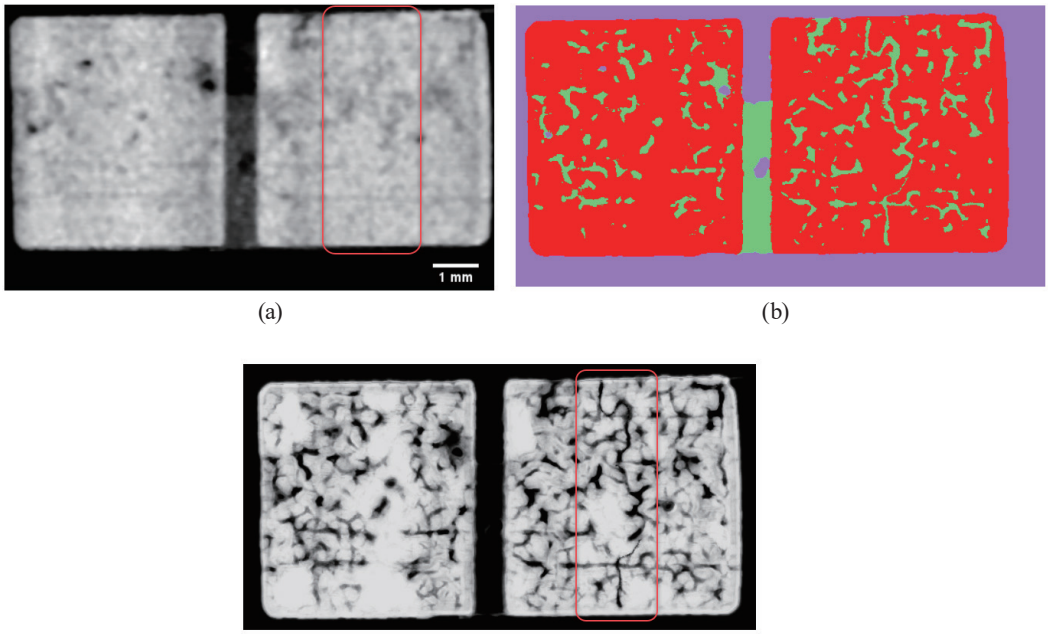

Fig. 6. (Color online) ML-based image segmentation of sample 1: (a) greyscale 2D CT image, (b) segmented 2D CT image, and (c) probability map of the segmented 2D CT image.

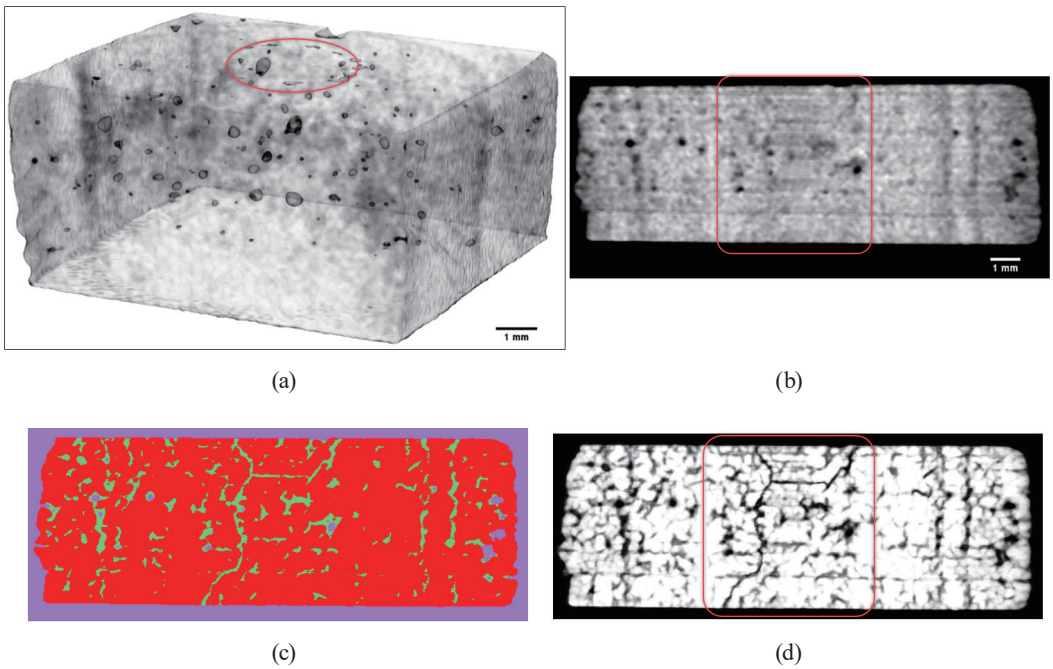

Fig. 7. (Color online) ML-based image segmentation of sample 2: (a) 3D CT image, (b) cross-sectional 2D CT image, (c) segmented 2D CT image, and (d) probability map of the segmented 2D CT image.

depicted in the side-view 3D CT image in Fig. 8(a). The varying shades of grey illustrate the distribution of the impregnation resin within the ADC sample. We observed a discontinuity of the leakage path, as highlighted in Fig. 8(a), and the cross-sectional 2D CT image along the discontinuity indicates that the sealant resin was confined to a narrow region (approximately 40–130 μm) along the leakage path. The low-viscosity super sealant resin might have drained from the comparatively significant defects along the leakage path during the standard impregnation technique.

We used the pretrained ML classifier of TWS to segment the 2D CT image of sample 3. This process enhanced the visibility of the sealant resin within the confined section of the leakage path, as depicted in Fig. 9(a). Furthermore, a close examination of the magnified image in Fig. 9(a) revealed the entrapment of minute air pockets within the impregnated sealant. Such trapping of air can be attributed to several factors, including polymerization shrinkage of the resin during the hardening process and the moisture within the sealant resin. The probability map in Fig. 9(b) further complements our understanding of the die-casting leakage path of Al alloy sample 3.

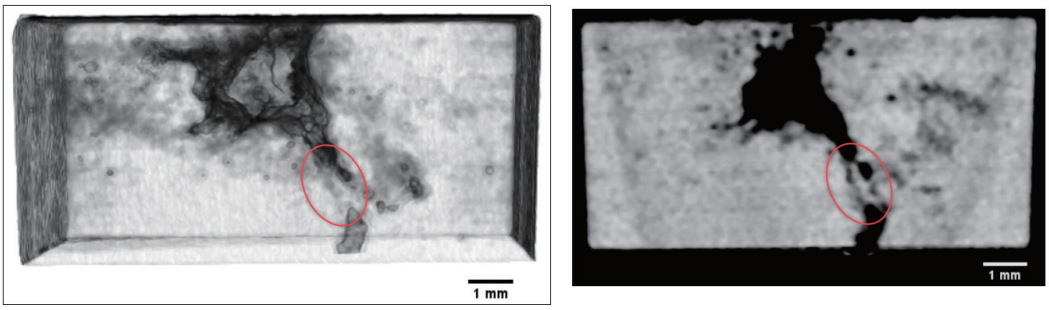

(a) (b)

Fig. 8. (Color online) XCT images of ADC sample 3: (a) side-view 3D CT image and (b) cross-sectional 2D CT image across the highlighted region of the 3D CT image.

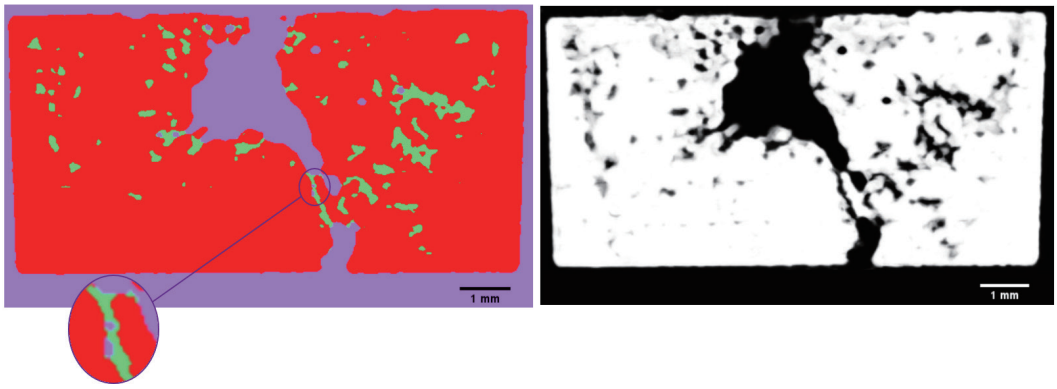

(a) (b)

Fig. 9. (Color online) ML-based image segmentation of sample 3: (a) segmented 2D CT image and (b) probability map of the segmented 2D CT image.

Therefore, the results of our qualitative analysis distinctly emphasize the merit of utilizing micro-XCT with direct conversion X-ray sensors to assess the efficacy of the impregnation process in sealing die-casting defects within industrial alloys.

3.2 Micro-XCT quantitative analysis

We employed the DXCT method with the photon-counting XCounter sensor to identify the impregnation sealant within Al alloy sample 1. We calculated the EANs of the sealant resin on the basis of the linear attenuation coefficients for the windows with low and high X-ray energies using Eq. (1) while considering the impregnation resin located within the center hole of sample 1. Figure 10 illustrates the obtained 2D CT images across the center hole containing the resin.

The low-atomic-number impregnation resin in the center hole is barely noticeable in the total-energy (20–140 keV) CT image. However, its visibility is significantly enhanced in the CT images captured in the low-energy (20–30 keV) and high-energy (50–60 keV) windows, as highlighted in Figs. 10(b) and 10(c), respectively. The calculated EANs are shown in Table 2.

The experimentally determined EAN ($Z_{eff(exp)}$) for the impregnation resin in sample 1 was 7.36, whereas the theoretical EAN ($Z_{eff(th)}$) for P601 is 7.10. Hence, the results obtained from the DXCT investigation provide quantitative validation, affirming that the properties of the impregnated material within the center hole of Al alloy sample 1 closely match those of P601 Super Sealant, with an error margin of only 3.53%. In the XMuDat method, 2-HEMA is considered to be the only chemical component of the P601 resin in the $Z_{eff(th)}$ calculation.

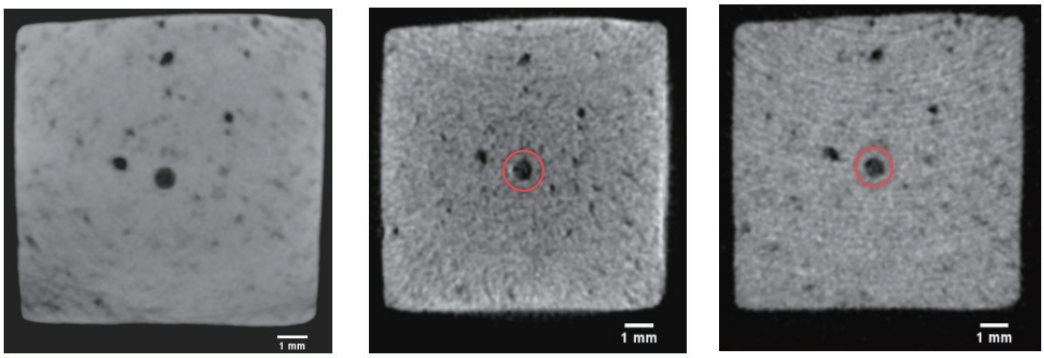

(a) (b) (c)

Fig. 10. (Color online) DXCT of ADC12 sample 1: (a) total-energy 2D CT image, (b) low-energy 2D CT image, and (c) high-energy 2D CT image.

Table 2
Comparison of experimental and theoretical EANs of Super Sealant P601 impregnation resin.

	μ (E_1) Low energy	μ (E_2) High energy	$Z_{eff(exp)}$	$\frac{(Z_{eff(exp-P601)} - Z_{eff(th-P601)})}{Z_{eff(exp-P601)}}$
ADC12 sample 1 ($Z_{eff(th)}$ of P601 = 7.10)	1.00×10^{12}	4.34×10^{11}	7.36	3.53%

However, P601 Super Sealant employs various bifunctional monomers for cross-linked polymerization, which makes the assumption used in the calculation of $Z_{eff(th)}$ insufficient, leading to a minor deviation from the experimental value.

4. Conclusions

Lightweight die-cast Al alloys play a leading role in many industrial applications because of their robust properties. However, inevitable casting defects have increased the rate of casting scraps and prevented the use of die-cast components in practical applications where air-tightness is mandatory. Therefore, VPI is applied as a cost-effective method to eliminate die-casting cracks and leakage paths, allowing the reuse of alloy products by improving their overall performance. Hence, evaluating the efficacy of the impregnation treatment in sealing casting defects is vital. We successfully conducted such an evaluation using a laboratory-based micro X-ray CT system. The advanced CdTe flat panel sensors, which can directly convert X-ray photons into electrical charge, were excellent for nondestructively visualizing the internal geometry and die-casting defects within the Al alloys. The distribution of the low-atomic-number impregnation resin was illustrated by adjusting the scalar opacity mapping in the 3D CT images. Identification of the sealant resin in subtle die-casting defects with traditional intensity thresholding was challenging in the 2D CT images due to their lower X-ray attenuation and several image artifacts, resulting in a low image quality measure of 6.26 between air and resin. The ML-based image segmentation approach with TWS was employed to effectively segment the CT image into three predefined classes. After adequately training the TWS tool with a known dataset, it automatically and accurately detected and segmented the low-atomic-number impregnation sealant within subtle die-casting defects. A perfectly sealed minute leakage path (20–50 μm) in Al alloy sample 2 was depicted in the segmented 2D CT cross-sectional image. The geometry of the leakage path and the polycrystalline nature of the ADC12 alloy were also effectively represented in segmented probability map images. Al alloy sample 3 was thus revealed to contain an uneven leakage path with a significant die-casting crack. Note that impregnation material was found only within a narrow section of the path, suggesting potential discharge from the leakage path during the standard VPI process. The ML-based segmented image revealed tiny air pores within the sealant resin, which can also affect the impregnation efficacy. In the DXCT analysis, the impregnation material was quantitatively recognized as the P601 Super Sealant from its EAN. Hence, the outcomes of this study confirm the effectiveness of industrial micro-XCT combined with advanced X-ray sensors to comprehensively verify the impregnation efficacy in sealing defects within lightweight die-cast alloys.

Acknowledgments

We wish to express our gratitude to the members of ANSeeN Inc. for their technical and instrumental support in conducting the XCT.

References

1 S. T. Neel and R. N. Yancey: Rev. Prog. Quant. Nondestr. Eval. **15** (1996) 497.
2 S. Carmignato: Industrial X-ray computed tomography, W. Dewulf and R. Leach, Eds. (Springer International Publishing, Cham, Switzerland, 2017) 1st ed., Vol. 10, pp. 978–3. https://doi.org/10.1007/978-3-319-59573-3.
3 S. R. Stock: Int. Mater. Rev. **53** (2008) 129. https://doi.org/10.1179/174328008X277803.
4 J. G. Behnsen, K. Black, J. E. Houghton, and R. H. Worden: Materials (Basel) **16** (2023) 1259. https://doi.org/10.3390/ma16031259.
5 V. Gómez, H. Herazo, and E. S. Stuart: Precis. Eng. **60** (2019) 544 https://doi.org/10.1016/j.precisioneng.2019.06.007
6 F. Akman, R. Durak, M. F. Turhan, and M. R. Kaçal: Appl. Radiat. Isot. **101** (2015) 107.
7 C. Cao, M. F. Toney, T.-K. Sham,R. Harder, P. R. Shearing, X. Xiao, and J. Wang: Mater. Today **34** (2020) 132.
8 Y. Zhou, J. Chen, O. M. Bakr, and O. F. Mohammed: ACS Energy Lett. **6** (2021) 739.
9 T. Buzug: Computed Tomography (Springer, Berlin, Germany, 2008).
10 S. K. Kennedy, A. M. Dalley, and G. J. Kotyk: J. Mater. Eng. Perform. **28** (2019) 728. https://doi.org/10.1007/s11665-018-3841-5
11 J. Kastner: 6th Conf. Industrial Computed Tomography 2016 (iCT2016). Case Studies in Nondestructive Testing and Evaluation, 6 (Part B) (2016) 2. https://doi.org/10.1016/j.csndt.2016.05.007.
12 F. Garcia-Moreno, T. R. Neu, P. H. Kamm, and J. Banhart: Adv. Eng. Mater. **28** (2022) 201355. https://doi.org/10.1002/adem.202201355.
13 D. Liu and J. Tao: Adv. Mater. Res. **308**–**310** (2011) 785. https://doi.org/10.4028/www.scientific.net/AMR.308-310.785.
14 W. J. Joost and P. E. Krajewski: Scr. Mater. **128** (2017) 107.
15 H. Juergen and T. Al-Samman: Acta Mater. **61** (2013) 818.
16 F. Campbell (Ed.): Lightweight Materials: Understanding the Basics (ASM International: Novelty, OH, USA, 2012).
17 J. Relland, L. Bax, and M. A. Ierdes: Vision on the Future of Automotive Lightweighting Alliance (Surrey, UK, 2019).
18 F. Czerwinski: Materials **14** (2021) 6631. https://doi.org/10.3390/ma14216631
19 NADCA Product Specification Standards for Die Casting, Publication #402 (Arlington Heights, IL, North American Die Casting Association, 2018) 10th ed.
20 D. Blondheim and A.Monroe: Int. J. Metalcast. **16** (2022) 330. https://doi.org/10.1007/s40962-021-00602-x.
21 L. Lattanzi, A. Fabrizi, A. Fortini, M. Merlin, and G. Timelli: Procedia Struct. Integrity **7** (2017) 505. https://doi.org/10.1016/j.prostr.2017.11.119
22 K. Kan, Y. Imura, H. Morii, K. Kobayashi, T. Minemura, and T. Aoki: World J. Nucl. Sci. Technol. **3** (2013) 106.
23 A. Bandara, K. Kan, H. Morr, A. Koike, and T. Aoki: Prod. Eng. Res. Devel. **14** (2020) 147. https://doi.org/10.1007/s11740-019-00946-8.
24 N. Soga, A. Bandara, K. Kan, A. Koike, and T. Aoki: Prod. Eng. Res. Devel. **15** (2021) 885. https://doi.org/10.1007/s11740-021-01071-1.
25 K. Yusuke, A. Bandara, N. Soga, K. Kan, A. Koike, and T. Aoki: Prod. Eng. Res. Devel. **17** (2023) 291. https://doi.org/10.1007/s11740-022-01147-6.
26 A. D. Plessis and P. Rossouw: Case Stud. Nondestruct. Test Eval. (2015). https://doi.org/10.1016/j.csndt.2015.03.001
27 A. Buratti, J. Bredemann, M. Pavan, R. Schmitt, and S. Carmignato: Applications of CT for dimensional metrology. In: S. Carmignato, W. Dewulf, and R. Leach (Eds.) Industrial X-ray computed tomography (Springer, Cham. 2018) pp. 333–369.
28 J. Kastner and C. Heinzl: X-ray computed tomography for nondestructive testing and materials characterization. In: Liu Z, Ukida H, Ramuhalli P, Niel K (Eds.) Integrated imaging and vision techniques for industrial inspection (Springer, London, 2015) p. 227.
29 C. Reinhart: 17th World Conf. Nondestructive Testing, Shanghai, China eJNDT **13** (2008) 25.
30 A. Thompson and R. Leach: Introduction to industrial X-ray computed tomography. In: S. Carmignato, W. Dewulf, and R. Leach (Eds.) Industrial X-ray computed tomography (Springer, Cham, 2018) pp. 1–23.
31 H. Randolf, T. Fuchs, and N. Uhlmann: Nucl. Instrum. Methods Phys. Res., Sect. A **591** (2008) 14.
32 M. A. Krueger, S. S. Huke, and R. W. Glenny: CircRes **112** (2013) e88. https://doi.org/10.1161/CIRCRESAHA.113.301162.

33 J. Maiora and M. Graña: The 2012 Int. Joint Conf. Neural Networks (IJCNN) Brisbane, Australia, June 10–15 (IEEE Explore, 2012) pp. 1–7.
34 W. Macdonald and S. Shefelbine: Med. Biol. Eng. Comp. **51** (2013) 1157.
35 B. Mutiargo, A. Garbout, and A. A. Malcolm: Proc. SPIE 11050, Int. Forum Medical Imaging in Asia 2019 (27 March 2019) 110500L. https://doi.org/10.1117/12.2521768
36 A. Kyrieleis, V. Titarenko, M. Ibison, T. Connolley, and P. J. Withers: J. Microsc. **241** (2010) 69.
37 J. Muders, J. Hesser, A. Lachner, and C. Reinhart: Int. Symp. Digital Industrial Radiology and Computed Tomography (Berlin, Germany, 2011).
38 J. Schindelin, I. Arganda-Carreras, E. Frise, V. Kaynig, M. Longair, T. Pietzsch, S. Preibisch, C. Rueden, S. Saalfeld, B. Schmid, J. Y. Tinevez, D. J. White, V. Hartenstein, K. Eliceiri, P. Tomancak, and A. Cardona: Nat. Methods **9** (2012) 676. https://doi.org/10.1038/nmeth.2019
39 R. Kikinis, S. D. Pieper, and K. Vosburgh: 3D slicer: a platform for subject-specifc image analysis, visualization, and clinical support. In: F. A. Jolesz (Ed.) Intraoperative imaging image-guided therapy **3** (2014) 277.
40 M. Reiter, D. Weiß, C. Gusenbauer, M. Erler, C. Kuhn, S. Kasperl, and J. Kastner: Proc. 5th Conf. Industrial Computed Tomography (iCT 2014) (Wels, Austria, NDT.net) pp. 273–282.
41 I. Arganda-Carreras, V. Kaynig, C. Rueden, K. W. Eliceiri, J. Schindelin, A. Cardona, and S. H. Seung: Bioinformatics **33** (2017) 2424. https://doi.org/10.1093/bioinformatics/btx180
42 D. F. Jackson and D. J. Hawkes: Phys. Rep. **70** (1981) 169.
43 D. J. Hawkes and D. F. Jackson: Phys. Med. Biol. **25** (1980) 1167.
44 R. Nowotny: XMuDat: photon attenuation data on PC. IAEA-NDS-195 (International Atomic Energy Agency, Vienna, Austria, 1998). http://www.mds.iaea.or.at/reports/mds-195.htm.